Energy transfer mechanisms in backward scattering of Cs^+ ions from N_2 molecules

S. Kita [1,*] T. Hattori,[1] and H. Tanuma [2]

[1]*Graduate School of Engineering, Nagoya Institute of Technology, Nagoya 466-8555, Japan*

[2]*Department of Physics, Faculty of Science, Tokyo Metropolitan University, Tokyo 192–0397, Japan*

(Received 4 September 2023; accepted 12 February 2024; published 1 March 2024)

The energy transfer processes in Cs^+-N_2 collisions were experimentally studied at laboratory (lab) collision energies $E_{lab} = 50-250$ eV and lab scattering angles $\theta > 2^\circ$ via differential scattering spectroscopy. A classical trajectory calculation method was used to analyze the experimental results. We observed specific electronic excitations to the $Cs^+ + N_2(A^3\Sigma)$ and $Cs^+ + N_2(a^1\Pi)$ states in the energy-transfer spectra with significant excitation probabilities in backward scatterings at lower center-of-mass (CM) energies $E = 13.6-18.3$ eV ($E_{lab} = 78-105$ eV) and a CM angle $\Theta \sim 165^\circ$ ($\theta = 5^\circ$). The results of the simulations of energy transfer spectra through classical trajectory calculations indicate that electronic transitions occur around the molecular orientation $\gamma = \pi/2$ and at vibrotational excitation energies $\Delta E/E < 0.12$. The potential crossings for the $N_2(A^3\Sigma)$ and $N_2(a^1\Pi)$ excitations are located at the intermolecular potentials of $V_{IM}(R, \gamma = \pi/2) = 13.4$ and 16.4 eV, respectively. $N_2(A^3\Sigma)$ excitation is the dominant electronic excitation process at lower energies of $E < 17.5$ eV ($E_{lab} < 100$ eV). Evaluations using an empirical charge-overlap model reasonably reproduce intermolecular potential crossings. Moreover the proposed model can provide effective information on the spin-changing $N_2(A^3\Sigma)$ excitation.

DOI: 10.1103/PhysRevA.109.032803

I. INTRODUCTION

Measurements of differential cross sections (DCSs) in atomic and molecular collisions provide effective information on energy transfer mechanisms. Collisions between closed-shell atoms and ions, such as rare-gas atoms (Rg) and alkali ions (M^+), have been studied by measuring the energy transfer spectra. One- and two-electron (1e and 2e) excitations have been observed simultaneously in Rg–Rg [1] and M^+–Rg [2–4] collisions. Excitations occur through rotational and radial couplings [5,6]. Most excitations proceed through radial couplings around the potential crossings at distances R_C and potential heights $V(R_C)$. We have extensively studied experimentally excitation processes in moderate-energy M^+–Rg collisions using a crossed beam apparatus [7]. The results were discussed by referring to *ab initio* calculations, electron promotion models, and empirical model potentials [8–10]. These studies were expected to provide information on the electronic excitation processes in M^+-N_2 collisions. Excitations in M^+–Rg collisions were observed at $V(R_C) > 35$ eV [7,8,10–12]. The excitation probabilities P_{ex} depend strongly on the collision systems; P_{ex} is high for quasisymmetric Li^+–He, Na^+–Ne, and K^+–Ar systems. For M^+–Ar systems, excitations with moderate or high P_{ex} were observed in Li^+–Ar and K^+–Ar collisions at the laboratory (lab) energies of $E_{lab} > 100$ eV. Meanwhile, those in Na^+–Ar collisions were observed with lower P_{ex} at higher energies of $E_{lab} > 500$ eV. Furthermore, exclusive 2e excitation with a higher P_{ex} was observed at $E_{lab} > 400$ eV for the heavier Cs^+–Ar system rather than 1e excitation.

The energy transfer processes in the molecular M^+-N_2 collisions of closed-shell systems have also been experimentally studied via differential scattering spectroscopy. In Li^+-N_2 and K^+-N_2 collisions [13,14], electronic 1e and 2e excitations were observed (similar to atomic systems) in addition to the momentum transfer (vibrotational excitations) of N_2 molecules. Electronic excitations in the Li^+-N_2 system were observed at $E_{lab} > 100$ eV and laboratory angle $\theta < 50^\circ$ [intermolecular potential height $V_{IM}(R_C) = 28$ eV], and those in the K^+-N_2 system were observed at $E_{lab} > 200$ eV and $\theta < 10^\circ$ [$V_{IM}(R_C) \sim 15$ eV]. The $V_{IM}(R_C)$ is approximately related to the reduced threshold angle $E_{lab}\theta_{th}$ in small angle scattering. With reference to the one-electron excitations of the N_2 molecules, electronic transitions to the $a^1\Pi$ state with excitation energy $\Delta E_{el} = 9.2$ eV and the $a'^1\Sigma$ (or $w^1\Delta$) state with $\Delta E_{el} = 10.3$ eV were observed in the impulsive Li^+-N_2 and K^+-N_2 collisions, respectively. The excitations occurred owing to vertical electronic transitions around the equilibrium distance r_e of the N_2 molecules. Furthermore, the excitation of the N_2 molecules to the $a^1\Pi$ state was observed in the impulsive He–N_2 collisions at $E_{lab} = 1.0$ keV and $0.2^\circ \leqslant \theta \leqslant 2.0^\circ$ [15]. Meanwhile, significant electronic excitation was not observed in Na^+-N_2 collisions at $E_{lab} < 350$ eV. The rotational and vibrational excitation processes in forward scattering, which is defined in Eq. (1), have been studied extensively [16–19]. Rotational excitations into the higher energy levels with higher probabilities for the Na^+-N_2 system were observed. This is expressed as the rotational rainbow [20–22] that appears at the molecular orientation of $\gamma_0 \sim 50^\circ$ (and 130°) defined at the turning point in the collisions [16]. Furthermore, the dissociative processes of N_2 molecules through the rotational excitations (angular momentum transfers) in Na^+-N_2 collisions were studied at $E_{lab} = 200$ and 350 eV

*Corresponding author: skita45@onyx.ocn.ne.jp

[19]. These studies indicate that the energy transfer by rotational excitations is equal in importance to that by vibrational excitations even at moderate energy collisions. The system dependence of the electronic excitations in M^+-N_2 collisions resembles that of M^+–Ar collisions [7,10,12].

This study experimentally investigated the energy transfer processes in the backward scattering of heavier Cs^+ ions from N_2 molecules at collision energies of $E_{lab} = 50-250$ eV, which correspond to center-of-mass (CM) energies of $E = 8.8$–43.6 eV. Electronic excitations of N_2 molecules into the $A^3\Sigma$ and $a^1\Pi$ states accompanied by vibrotational excitations were observed extensively at lower collision energies $E = 13.6-18.3$ eV ($E_{lab} = 78-105$ eV) and a large CM angle $\Theta \sim 165^\circ$ ($\theta = 5^\circ$). The threshold collision energies for these excitations were observably lower than those for the atomic M^+–Rg collisions. The spin-changing $N_2(X^1\Sigma) \rightarrow N_2(A^3\Sigma)$ transition proceeds through spin-orbit coupling [23] between the electronically excited quasimolecular $(CsN_2)^{+*}$ states. The experimental energy transfer spectra were analyzed using the classical trajectory calculation (CT) method [16,24]. Furthermore, the intermolecular potential crossings between the ground and excited states were evaluated using the empirical charge-overlap model [10] to understand the lower threshold energies for electronic excitations.

II. EXPERIMENTAL DETAILS

A. Apparatus

Differential scattering measurements were performed using a crossed-beam apparatus [7,25]. Primary Cs^+ ion and secondary N_2 beams crossed perpendicularly at the scattering center. The primary Cs^+ ions were produced through thermionic emission and accelerated to the desired energies. A supersonic N_2 beam with a mean velocity of $V_0 = 7.85 \times 10^4$ cm/s was used as the secondary target beam [26]. The scattering lab angle θ was determined with respect to the primary ion-beam axis. The Cs^+ ion beam for the time-of-flight (TOF) measurements was pulsed using a pair of condenser plates [27]. The flight path length from the scattering center to the detector was approximately $L_f = 49.5$ cm. The time resolutions $\Delta T/T$ in the TOF measurements were approximately 1/300–1/800 full width at half maximum (FWHM) for ion energies of $E_{lab} = 50-250$ eV and scattering angle of $\theta = 2^\circ$. The overall angular resolution of the scattered particles was 0.2°–0.5° FWHM. At lower energies around $E_{lab} = 50$ eV, the measurements were performed under lower angular and time resolutions ($\Delta\theta \sim 0.5^\circ$ and $\Delta T/T \sim 1/300$) to overcome the lower scattered intensity. In our experiments the scattered Cs^+ ions were detected using a secondary electron multiplier composed of Cu-BeO dynodes (detection efficiency $\varepsilon = 1$) [8].

B. Differential scattering measurements

The intensity $I(\theta)$ of the particles scattered at a lab angle θ corresponded to the relative DCS $\sigma(\theta)$. In this study, collision experiments were performed at lab energies $E_{lab} = 50-250$ eV and angles $\theta > 2^\circ$. In the Cs^+-N_2 collision system, the mass of the Cs^+ ions ($m = 132.9$ u) was significantly larger than that of the target N_2 molecules ($M = 28.0$ u).

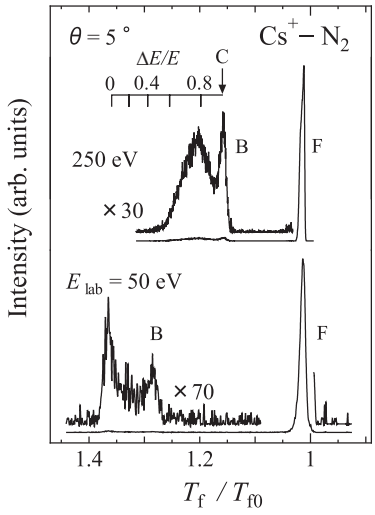

FIG. 1. TOF spectra measured at collision energies of $E_{lab} = 50$ and 250 eV, and scattering angle of $\theta = 5^\circ$. The abscissa indicates the reduced flight time T_f/T_{f0}, where T_{f0} denotes the flight time of the incident beam. The signals F and B correspond to forward and backward scatterings, respectively. The scale $\Delta E/E$ and arrow C denote the reduced energy transfer and cutoff energy position [$(\Delta E/E)_C = 0.861$], respectively, for backward scattering at $E_{lab} = 250$ and $\theta = 5^\circ$.

Moreover, scattered ions were observed only at smaller angles $\theta < 14^\circ$, which was owing to the kinematical effect [see Eq. (1)], as observed in the Na^+-N_2 [18] and K^+-N_2 collisions [28]. The magnitudes of the DCSs $\sigma(\theta)$ were determined using the calculated statistical potential. This is explained in detail in Sec. III.

1. TOF measurements

The velocities of the scattered particles were analyzed using the time-of-flight technique. Figure 1 shows the TOF spectra of the scattered Cs^+ ions measured at the collision energies of $E_{lab} = 50$ and 250 eV and a scattering angle of $\theta = 5^\circ$. The abscissa indicates the normalized flight time T_f/T_{f0}, where T_{f0} indicates the flight time of the incident ion beam. Furthermore, the intensive peak F and weak peak B represent the forward and backward scattering signals, respectively. Under our experimental conditions, the velocity v_p of scattered projectiles at a lab angle θ is given by [25]

$$v_P = \frac{mv_0}{m+M}\left\{\cos\theta + \frac{MV_0}{mv_0}\sin\theta \pm \left[\left(\cos\theta + \frac{MV_0}{mv_0}\sin\theta\right)^2 - \frac{m^2-M^2}{m^2} - \frac{M^2\Delta E}{m^2 E}\right]^{\frac{1}{2}}\right\}, \quad (1)$$

where m and M are the masses of the projectile and target, respectively; v_0 and V_0 are the initial velocities of the projectile and target, respectively; and $\Delta E/E$ is the reduced excitation energy. Terms with the sign $\pm$ in Eq. (1) correspond to forward scattering (CM angle $\Theta_F < \Theta_C$), and backward scattering ($\Theta_B > \Theta_C$), respectively, where Θ_C is the cutoff angle in the CM system. The cutoff angle θ_C in the lab system is defined

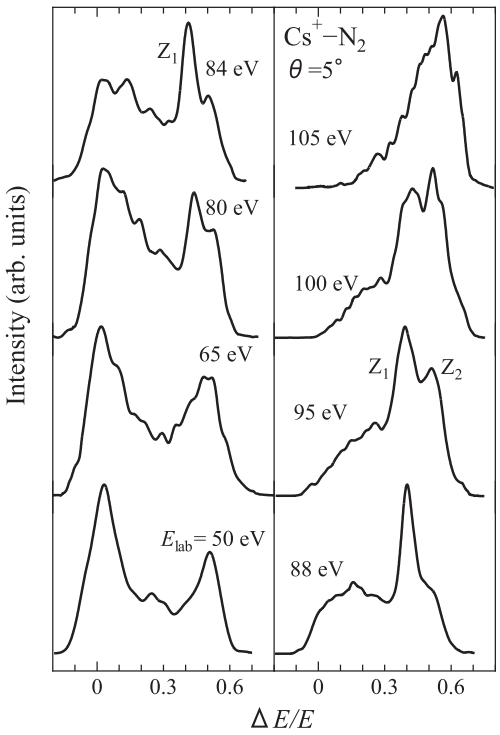

FIG. 2. Collision energy dependence of energy transfer spectra for backward scattering in the lab system measured at $E_{lab} = 50$–105 eV and $\theta = 5°$. The energy transfer spectrum structures observed at $E_{lab} = 50$ and 65 eV are because of typical rotational and vibrational excitations. An additional peak signal Z_1 is observed at collision energies of $78 \leqslant E_{lab} \leqslant 100$ eV, whereas another signal Z_2 is observed at $E_{lab} = 95$–100 eV.

by the zero condition of the square root in Eq. (1). Assuming a stationary target, the cutoff angle for elastic scattering is given by $\theta_C = \sin^{-1}(M/m) = 12.2°$, whereas the CM angle $\Theta_C = \cos^{-1}(-M/m) = 102°$ [29]. Thus, we have two types of signals at a certain angle $\theta < \theta_C$. The backward signals for $E_{lab} = 50$ and 250 eV in Fig. 1 were intensified by factors of 70 and 30, respectively. The $\Delta E/E$ scale yields the reduced energy transfer for backward scattering at $E_{lab} = 250$ eV and $\theta = 5°$. Thus, a larger time-of-flight corresponds to a lower energy transfer $\Delta E/E$ for backward scattering. The arrow C indicates the largest energy transfer (cutoff energy) position for backward scattering determined kinematically by

$$\left(\frac{\Delta E}{E}\right)_C = 1 - \left(\frac{m}{M}\right)^2 \sin^2\theta + \frac{mV_0}{Mv_0} \sin 2\theta. \qquad (2)$$

The cutoff energy $(\Delta E/E)_C$ corresponds to the energy transfer at the cutoff angle θ_C, which also originated from the zero condition of the square root in Eq. (1). For $E_{lab} = 250$ eV and $\theta = 5°$, the energy transfer $(\Delta E/E)_C$ is approximately 0.861. In an additional high-energy measurement at $E_{lab} = 350$ eV (and $\theta = 5°$), the gross features of the TOF spectrum were almost identical to those for $E_{lab} = 250$ eV.

2. *Energy transfer spectra*

Figure 2 shows the energy transfer spectra determined from the backward-scattering signals in the TOF spectra

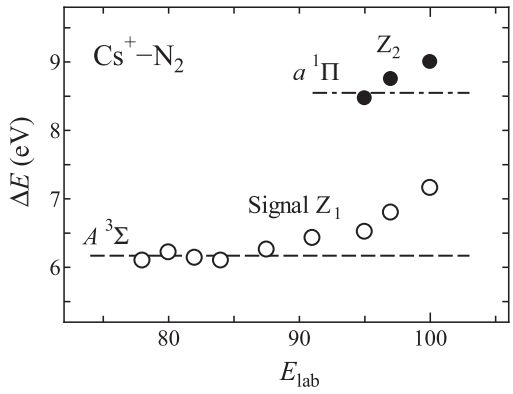

FIG. 3. Collision energy dependences of peak positions of signals Z_1 and Z_2 observed in the experimental spectra in Fig. 2. The dashed and dot-dashed lines indicate the excitation energies for electronic transition into the $N_2(A^3\Sigma)$ ($\Delta E_1 = Q_1 = 6.17$ eV) and $N_2(a^1\Pi)$ ($\Delta E_2 = Q_2 = 8.55$ eV) states, respectively, of the N_2 molecules, where Q_i denotes the electronic excitation energy.

measured at $E_{lab} = 50$–105 eV and $\theta = 5°$. The elastic scattering signal in the Cs^+–Ar collisions was used to determine the elastic position ($\Delta E/E = 0$) in the energy-transfer spectra of the Cs^+–N_2 collisions. Furthermore, the backward-scattering signals had weak noise intensities (Fig. 1). Therefore, the evaluated energy transfer spectra were convoluted using Gaussian functions with widths $d = 0.4$–0.6 eV FWHM, which depended weakly on the collision energy ($d = 0.4$ eV at $E_{lab} \leqslant 65$ eV. The energy transfer spectra for the backward-scattering measured at a lab angle $\theta = 5°$ are discussed in this paper. As observed in the figure, the spectra are almost identical at the lower energies $E_{lab} = 50$ and 65 eV, whereas additional signals Z_1 and Z_2 are observed in the spectra at $E_{lab} \geqslant 78$ eV. As shown in Figs. 1 and 2, the energy transfer $\Delta E/E$ increased as the collision energy increased. This study primarily discussed the energy transfer processes in the backward scattering at $E_{lab} = 50$–105 eV.

Figure 3 shows the collision energy dependence of the energy transfer ΔE for the additional signals Z_1 and Z_2. At $E_{lab} = 78$–88 eV the ΔE of the signal Z_1 (ΔE_{Z1}) has an almost constant value of approximately 6.2 eV. Meanwhile, at $E_{lab} > 90$ eV, ΔE_{Z1} increases slightly as E_{lab} increases. The energy $\Delta E_{Z1} \sim 6.2$ eV nearly equals the electronic excitation energy $Q_{Z1} = 6.17$ eV for the transition $N_2(X^1\Sigma)(v = 0) \rightarrow N_2(A^3\Sigma)(v' = 0)$ of N_2 molecules [30,31], where v and v' are vibrational quantum numbers. The singlet–triplet transition is generally prohibited for closed-shell systems, such as lighter systems of Li^+–N_2 and K^+–N_2 [13,14]. This is based on the Wigner spin conservation rule. The reaction observed in our experiments for the heavier Cs^+–N_2 system is interpreted to proceed through a spin-orbit coupling interaction [23,32,33] between the electronically excited quasimolecular $(CsN_2)^{+*}$ states. This is discussed in Sec. V B 2. Conversely, the energy transfers ΔE_{Z2} for the signal Z_2 observed at $E_{lab} \geqslant 95$ eV are close to the electronic excitation energy $Q_{Z2} = 8.55$ eV for the transition $N_2(X^1\Sigma)(v = 0) \rightarrow N_2(a^1\Pi)(v' = 0)$ [30,31]. Thus, the additional signals Z_1 and Z_2 can be attributed to the electronic transitions into the $N_2(A^3\Sigma)$ and $N_2(a^1\Pi)$ states. Furthermore, the energy transfers of the signals Z_1 and Z_2

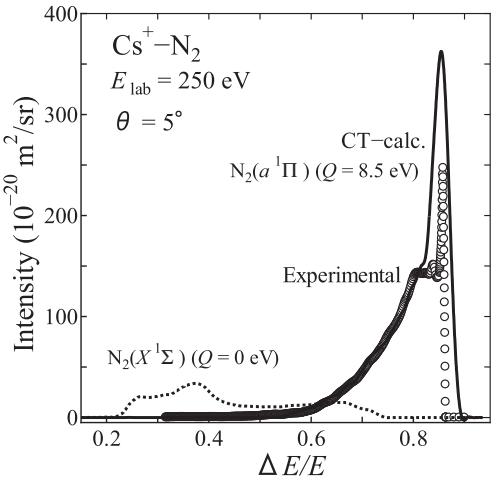

FIG. 4. Energy transfer spectra for backward scattering in the lab system determined experimentally and simulated by classical trajectory (CT) calculation at energy E_{lab} =250 eV and angle θ = 5°. The open circles and solid curve denote the experimental and simulated spectra, respectively. The calculation was performed for the electronic transition to the $Cs^+ + N_2(a^1\Pi)$ state with excitation energy Q = 8.5 eV. The dotted curve shows the CT calculation for the electronic ground state with Q = 0 for comparison.

in Fig. 3 are represented by $\Delta E_i(E_{lab}) = Q_i + \Delta\varepsilon_i(v_i\prime,\ E_{lab})$, where Q_i and $\Delta\varepsilon_i(v_i\prime,\ E_{lab})$ are the electronic and vibrational excitation energies, respectively. According to the discussion in Sec.VA, the contribution of the rotational excitation was omitted in this study.

Figure 4 shows the energy-transfer spectrum for the backward scattering signals measured at E_{lab} = 250 eV and θ = 5°. The experimental spectrum shown by open circles has a sharp quasi-rainbow peak around $\Delta E/E$ = 0.86 originating from the cutoff structure in the TOF spectrum shown in Fig. 1. The intensities of the experimental energy-transfer spectra at larger energy transfers $\Delta E/E$ are strongly influenced by the kinematical $\Delta E/E$ dependence in the Jacobian factor $J(\theta) = d\Omega_{CM}/d\Omega_{lab}$, where $d\Omega_{CM}$ and $d\Omega_{lab}$ are infinitesimal solid angles for the CM and lab frames, respectively. Omitting the contribution from the initial target velocity to simplify our discussion, the Jacobian is given by $J(\theta) = J(\Theta)^{-1} = (1+\gamma^2+2\gamma\cos\Theta)^{3/2}/(1+\gamma\cos\Theta)$, with $\gamma = (m/M)(1–\Delta E/E)^{-1/2}$ [29]. Thus, $J(\theta)$ has a singularity peak (quasi-rainbow) at the cutoff energy $(\Delta E/E)_C$ = 0.861 and CM angle $\Theta_C = \cos^{-1}(-1/\gamma) = 94.5°$, as shown in this figure. Therefore, the energy-transfer spectra in the laboratory system were transformed into spectra in the CM system to eliminate the kinematic effect.

The energy-transfer spectra for backward scattering signals measured at E_{lab} = 50–105 eV and θ = 5° were transformed into a CM system. The lab angle θ = 5° was approximated to the CM angle Θ = 165°. This was because θ = 5° corresponds to Θ = 160–170° under our experimental conditions. The energy transfer spectra in the CM system for E_{lab} = 50 and 84 eV are shown in Fig. 5. This study exclusively discussed backward scattering at a CM angle of Θ = 165° (lab angle θ = 5°).

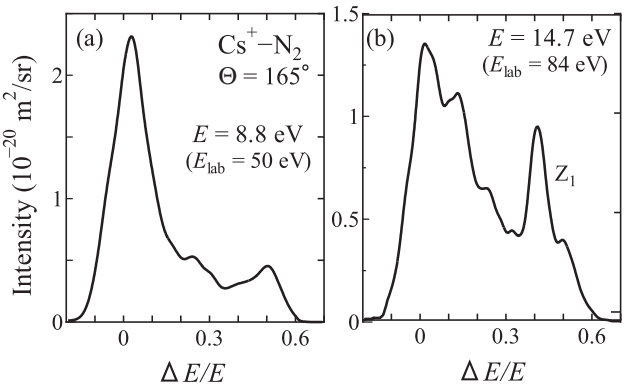

FIG. 5. Experimental energy transfer spectra for backward scattering in the CM system. (a) At CM energy E = 8.8 eV (E_{lab} = 50 eV) and angle Θ = 165° (θ =5°) and (b) at E = 14.7 eV (E_{lab} = 84 eV) and Θ = 165° (θ =5°).

III. REPULSIVE POTENTIAL CALCULATIONS

The interaction potentials were calculated using a scaled statistical model to investigate the energy transfer mechanisms [34]. The intermolecular potentials under our experimental conditions were repulsive in the energy range $1 < V_{IM}(R) < 100$ eV. However, the repulsive potential of the Cs^+–N_2 system has not been reported. The interaction potential for closed-shell systems, such as the Rg–Rg and M^+–Rg systems, was reproduced effectively by the scaled statistical model. Furthermore, the potentials between M^+ ions (M^+ = Li^+, Na^+, and K^+) and N atoms provide reasonably good experimental potentials for molecular M^+–N_2 systems [35]. Because the correction factors δ_i for kinetic, exchange, and correlation energies in the scaled statistical model depend on the total number of electrons n in the interacting system [34], the factors δ_i of the Cs^+–N system were evaluated using interpolation procedures. Potential calculations were performed using charge densities $\rho_{i,j}$ for the Cs^+ ion and N atom determined from the Hartree-Fock wave functions [36]. Furthermore, the intermolecular potential $V_{IM}(R,\gamma)$ for the molecular system Cs^+–N_2 was evaluated by assuming the additive potentials of the Cs^+–N systems, $V_{IM}(R,\gamma) = V_A(r_1) + V_B(r_2)$, where γ is the angle between the vector $\boldsymbol{R}$ and the molecular axis, which is the molecular orientation. Figure 6 shows the geometrical parameters r_1–r_3, R, and

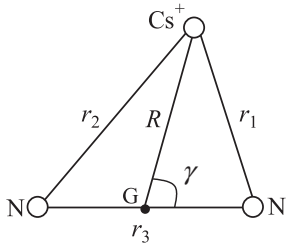

FIG. 6. Schematic of the coordinates for the Cs^+–N_2 system. The coordinates r_1 and r_2 are the interatomic Cs^+–N distances, and r_3 is the intramolecular N–N distance. R is the distance between the Cs^+ ion and the center of gravity G of the N_2 molecule, and γ is the orientation angle between the vector $\boldsymbol{R}$ and molecular axis.

TABLE I. Potential parameters for Cs^+-N_2 and Cs^+–CO systems evaluated using statistical potential model. The function $V_{IA}(r) = A\exp(-Br)$ provides the interatomic potentials at $1 < V_{IA}(r) < 100$ eV. The function $V_{IM}(R) = A\exp(-BR)$ provides the intermolecular potentials averaged over the molecular orientation angles γ and the potentials $V_{IM}(R, \gamma)$ for the orientation $\gamma = 0$ and $\pi/2$, at $1 < V_{IM}(R) < 100$ eV.

System	A (eV)	B (10^{10} m^{-1})
Cs^+–N	2450	3.30
Cs^+-N_2	5780	3.22
Cs^+-N_2 ($\gamma = 0$)	15 500	3.31
Cs^+-N_2 ($\gamma = \pi/2$)	2730	3.15
Cs^+–C	1700	3.13
Cs^+–O	3300	3.49
Cs^+–CO	5300	3.20

γ used to describe the interaction potentials. Furthermore, the intramolecular N–N distance r_3 equals the equilibrium distance r_e; that is, $r_3 = r_e = 1.098 \times 10^{-10}$ m [30] and the intramolecular potential $V_C(r_3) = 0$. Although the intermolecular potential used here is simple, it reproduced the *ab initio* potential $V_{IM}(R, \gamma)$ for the Li^+-N_2 system reasonably well [13]. The evaluated interatomic potentials $V_{A,B}(r_{1,2})$ and spherically averaged $V_{IM}(R)$ could be approximated effectively in an exponential form at $1 < V_{A,B}(r_{1,2})$ and $V_{IM}(R) <$ 100 eV. The potentials of the Cs^+–C, Cs^+–O, and Cs^+–CO systems were calculated for comparison. The N_2 and CO molecules are isoelectronic systems. The potential parameters for the interatomic $V_{IA}(r_{1,2})$, the intermolecular $V_{IM}(R)$, and the $V_{IM}(R, \gamma = 0$ and $\pi/2)$ at the orientations $\gamma = 0$ and $\pi/2$ are listed in Table I. The potential $V_{IM}(R) = 1$–100 eV for the Cs^+-N_2 and Cs^+–CO systems are almost identical (with a difference of a few percentage points). This is almost similar to the experimental results for the M^+($M^+ = Li^+$, Na^+, and K^+) $–N_2$ and –CO systems [37]. This occurs because the repulsive potentials for closed shell systems are strongly related to the numbers of electrons of the interacting particles [10]. The potential $V_{IM}(R)$ for the Cs^+-N_2 system is higher (∼35%) than the statistical and experimental potentials for the Cs^+-Ar system [10].

The total DCSs for the molecular collisions at small angles are represented by the elastic DCS evaluated using the spherical potential $V_{IM}(R)$ [18]. The DCSs measured in this study for Cs^+-N_2 collisions at $E_{lab} = 50-250$ eV were relative. The magnitude of the experimental DCSs were determined by normalizing the total DCS measured at small angles $\theta <$ 5° to the elastic DCS calculated using the spherical potential $V_{IM}(R)$ in Table I.

IV. DCS AND ENERGY TRANSFER SPECTRA CALCULATIONS

A. DCSs calculated using a classical trajectory method

The DCSs in the CM system were calculated using the CT method [16,24]. It considers the momentum transfer (vibrotational excitation) in the collisions. The interaction potential for the Cs^+-N_2 collision system was approximated using the following additive interaction:

$$W(r_1, r_2, r_3) = V_A(r_1) + V_B(r_2) + V_C(r_3), \tag{3}$$

where the distances $r_1 - r_3$ are defined in Fig. 6. The Cs^+–N interactions V_A and V_B are listed in Table I as the interatomic potentials V_{IA}. The N–N interaction V_C was approximated by the Morse function using the spectroscopic data [30]:

$$V_C(r_3) = D_e\{1 - \exp[-a(r_3 - r_e)]\}^2 + Q_e. \tag{4}$$

The potential parameters of the electronic ground-state potential $V_{C1}(r_3,\ X^1\Sigma)$; and electronically excited-state potentials $V_{C2}(r_3,\ A^3\Sigma)$ and $V_{C3}(r_3,\ a^1\Pi)$ are summarized in Table II(a). The potential parameters in the table are the dissociation energy D_e, exponential constant a, equilibrium intramolecular distance r_e, and excitation energy Q_e. The intramolecular potential crossing distances r_{3C} for the excited-state potentials discussed in Sec. V B 1 [Fig. 11(b)] are also indicated in the table.

CT calculations of the deflection functions for the CM systems using the vibrating-rotor model were performed as functions of the polar angle α, azimuth β (which define the molecular orientation in the space-fixed coordinate system), and vibrational initial phase η in addition to the impact parameter b, i.e., CM angle $\Theta(\alpha, \beta,\ \eta; b)$. The calculations were performed at the angles of $\alpha = \beta = 0$–π, $\eta = 0$–2π, and $\Delta b = (1.0$–$2.5) \times 10^{-12}$ m. Furthermore, the number of trajectories for the phase η was $n_\eta = 8$–16 in our calculations considering vibrational excitations in the backward scattering for the Cs^+-N_2 collisions depending on the initial phase η. Moreover, a period of the initial zero-point vibration was addressed by dividing it into n_η phases.

The DCSs $\sigma(\Theta)$ in the CM system were calculated by summing up the impact parameter $b(\alpha, \beta,\ \eta; \Theta)$ for α, β, and η at each angle Θ, using the following relation [18]:

$$\sigma(\Theta) = \frac{1}{N_0}\sum_{i=1}^{n(\Theta)} \frac{b_i(\alpha, \beta, \eta; \Theta)\Delta b}{\sin\Theta\Delta\Theta}, \tag{5}$$

where N_0 is the number of points selected for the molecular orientations α. β and vibrational initial phase η. The DCSs $\sigma(\Theta)$ were evaluated by sorting 2 00 000 trajectories of b (α, β, η; Θ) into bins of width $\Delta\Theta = 2°$ centered at each angle Θ. The calculated DCS $\sigma(\Theta)$ monotonically decreased as the angle increased. However, $\sigma(\Theta)$ had small constant values (within 10%) at large angles of $\Theta > 150°$. The $\sigma(\Theta)$ at $\Theta = 165°$ weakly depended on the collision energy, i.e., $\sigma(\Theta = 165°) = (0.52-0.46) \times 10^{-20}$ m^2/sr at $E = 8.8-18.3$ eV ($E_{lab} = 50$–105 eV). The DCS $\sigma(\Theta)_{CT}$ calculated at the small angles $\Theta < 60°$ using the CT methods was almost identical to the elastic DCS $\sigma(\Theta)_{EL}$ obtained using the spherical potential $V_{IM}(R)$ indicated in Table I. Meanwhile, at the large angle $\Theta = 165°$ and energies $E = 8.8$–18.3 eV, the DCS $\sigma(\Theta)_{CT}$ was moderately (∼15%) smaller than $\sigma(\Theta)_{EL}$. This should be owing to the multiple collision effect discussed in Sec. V A.

TABLE II. (a) Intramolecular potential parameters for the $N_2(X^1\Sigma)$, $N_2(A^3\Sigma)$, and $N_2(a^1\Pi)$ states, and potential crossing distances r_c evaluated from the data of Refs. [30] and [31]. The potentials are given by the Morse function of $V(r) = D_e\{1-\exp[-a(r-r_e)]\}^2 + Q_e$. (b) Intermolecular potential parameters for electronically excited states evaluated experimentally for the Cs^+-N_2 system at molecular orientation $\gamma = \pi/2$, and potential parameters at potential crossings. The potentials are given by $V_{IM}(R, \gamma = \pi/2) = A\exp(-BR) + Q$. The data in parentheses indicate crossing parameters evaluated using the charge-overlap model. H_{12} provides coupling energy at the potential crossing between the ground and excited states.

(a)

State	D_e (eV)	a (10^{10} m^{-1})	r_e (10^{-10} m)	Q_e (eV)	r_c (10^{-10} m)
$N_2(X^1\Sigma)$	9.905	2.689	1.098	0	–
$N_2(A^3\Sigma)$	3.681	2.732	1.287	6.224	1.24
$N_2(a^1\Pi)$	6.083	2.470	1.220	8.590	1.18

(b)

State	A (eV)	B (10^{10} m^{-1})	Q (eV)	Rc (10^{-10} m)	$V(R_C)$ (eV)	H_{12} (eV)
$Cs^+-N_2(A^3\Sigma)$	12 070	4.40	6.17	1.69 (1.62)	13.35 (16)	0.33
$Cs^+-N_2(a\ ^1\Sigma)$	2860	3.65	8.55	1.62 (1.50)	16.4 (24)	—

B. Energy transfer spectra through classical trajectory calculations

The energy transfer spectra at the CM energies of E = 8.8–18.3 eV (E_{lab} = 50–105 eV) and Θ =165° (θ = 5°) were calculated by CT methods using vibrating-rotor and rigid-rotor models. Trajectories of total numbers n = (2–5) × 10 000 that fell within the interval $\Delta\Theta = 2°$ were sorted into bins of width $\Delta(\Delta E/E) = 0.001$ or 0.005, and the raw spectra were convoluted using Gaussian functions for comparison with the experimental results. Figure 7 shows the energy transfer spectra in the CM frame at E = 8.8 eV (E_{lab} = 50 eV) and Θ = 165° (θ = 5°). In Fig. 7(a), the spectrum obtained by the vibrating-rotor model calculations is compared with that obtained experimentally, which is identical to Fig. 5(a). The solid curve shows the spectrum convoluted using the sum of double Gaussian functions with widths $w \equiv \Delta(\Delta E/E)$ = 0.04 and 0.14 FWHM. Thus, the simulated spectrum effectively reproduces the experimental result. The dashed curve represents the raw CT calculation. The rigid-rotor model spectrum is compared with the vibrating-rotor model spectrum in Fig. 7(b), to demonstrate the contribution of the rotational excitation in the vibrating-rotor model calculation, in which the abscissa has a narrow range of $\Delta E/E < 0.15$. The rigid-rotor model spectrum (solid curve) comprises a sharp peak around $\Delta E/E = 0$. Meanwhile, the vibrating-rotor model spectrum shown by the dotted curve in Fig. 7(b) has the appreciable onset energy of $(\Delta E/E)_{on} \sim 0.02$, which depends on the vibrational initial phase η. Therefore, the raw spectrum calculated using the vibrating-rotor model in Fig. 7(a) has a structure that is significantly broader than that of the rigid-rotor model spectrum at $\Delta E/E < 0.1$.

Figure 8 shows the spectra calculated using the vibrating rotor model and that determined experimentally in the CM frame at E = 14.7 eV (E_{lab} = 84 eV) and Θ = 165° (θ = 5°). Here the abscissa is given by ΔE to illustrate the absolute energy transfer, which is different from Fig. 5(b). The solid curve in Fig. 8(a) shows the CT spectrum convoluted using the sum of double Gaussian functions with widths w = 0.035 and 0.10 FWHM, and the dashed curve shows the raw CT spectrum. The experimental spectrum (open circles) has an additional signal Z_1. This is attributed to the electronic excitation into the $N_2(A^3\Sigma)$ state (excitation energy Q = 6.17 eV).

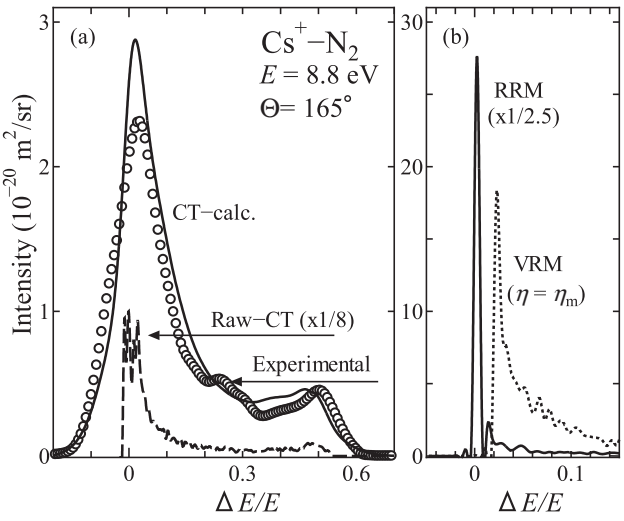

FIG. 7. (a) Energy transfer spectra simulated through CT calculation using the vibrating-rotor model (VRM) and determined experimentally at CM energy of E = 8.8 eV (E_{lab} = 50 eV) and CM angle of Θ = 165° (θ =5°). The solid curve denotes the spectrum convoluted using double Gaussian functions. The dashed curve denotes the raw spectrum decreased by a factor of 1/8. The circles denote the xperimental spectrum, and are identical to those in Fig. 5(a). (b) Spectra calculated by using a CT method in a narrow range of $\Delta E/E < 0.15$. The solid curve shows a rigid-rotor model (RRM) spectrum decreased by a factor of 1/2.5. The dotted curve denotes a vibrating-rotor model spectrum for a phase $\eta_m = 0.7\pi$ of zero-point vibration, which provides the highest onset energy of $\Delta E/E \sim 0.02$.

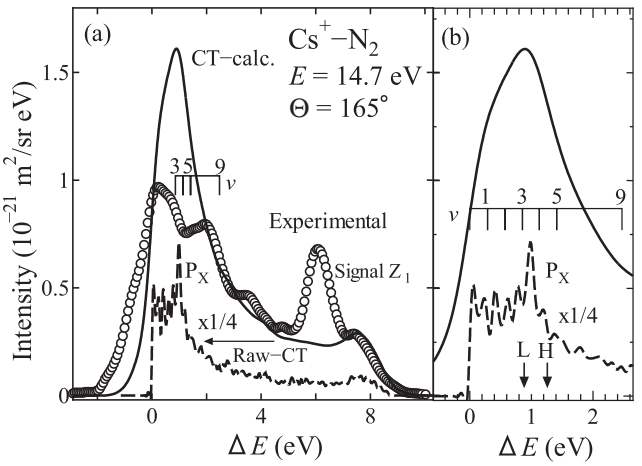

FIG. 8. Energy transfer spectra in the CM system simulated through CT calculation using the vibrating-rotor model and determined experimentally at $E = 14.7$ eV ($E_{lab} = 84$ eV) and $\Theta = 165°$ ($\theta = 5°$). (a) The solid and dashed curves show the convoluted and raw-CT spectra, respectively. The raw-CT spectrum decreases by a factor of 1/4. The experimental energy transfer spectrum shown by circles is identical to that in Fig. 5(b). The spectrum has an additional signal Z_1. It can be attributed to electronic excitation to the $N_2(A^3\Sigma)$ ($Q = 6.2$ eV) state. The energy scale v indicates the vibrational energy levels for the electronic transition $N_2(X^1\Sigma)$ ($v = 0$) → $N_2(X^1\Sigma)$ ($v \geqslant 3$) → $N_2(A^3\Sigma)$ ($v' = 0$). (b) Energy transfer spectra at a narrow range of $\Delta E < 2.6$ eV. The peak P_X in the raw-CT spectrum is related to the discussion of the electronic excitation process (Figs. 11 and 13). The arrows L and H denote the lowest and highest energy transfers ΔE_L and ΔE_H, respectively, used for the intensity evaluation of P_X.

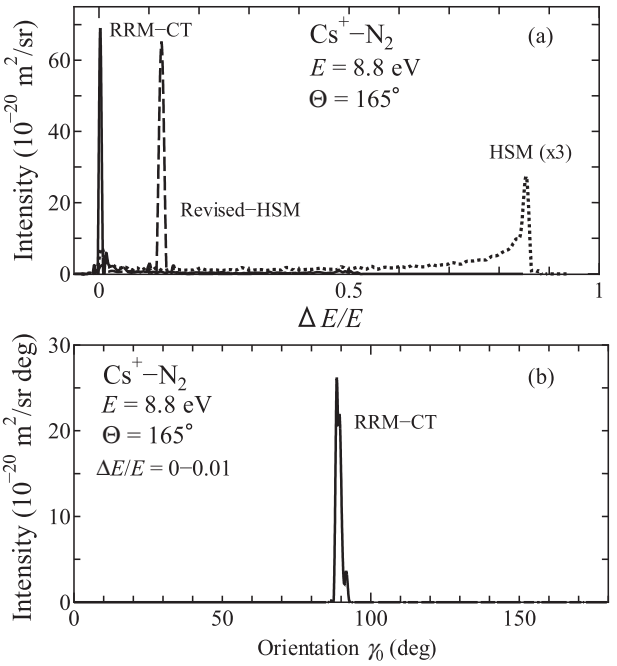

FIG. 9. (a) Energy transfer spectra evaluated at $E = 8.8$ eV ($E_{lab} = 50$ eV) and $\Theta = 165°$ using the CT rigid-rotor model (RRM-CT) and hard-shell model (HSM) calculations. The solid and dotted curves denote the RRM-CT and HSM spectra, respectively. The RRM spectrum (solid curve) is identical to that in Fig. 7(b). The dotted curve indicates the HSM spectrum multiplied by a factor of three. The dashed curve comprising a sharp peak at the energy transfer of $\Delta E/E = 0.13$ denotes the HSM spectrum revised considering angular momentum conservation. (b) Orientation γ_0 distribution of scattered intensity $I(\gamma_0)$ at the reduced energy transfer of $0 \leqslant \Delta E/E \leqslant 0.01$, which corresponds to a sharp peak position in the rigid-rotor model spectrum in Fig. (a). The prominent peak is located around $\gamma_0 = 89°$.

Thus, the contribution from the electronic excitation is observable, and the agreement between the vibrating-rotor model calculation and experiment is insufficient for the Cs^+-N_2 collisions at $E > 14.0$ eV ($E_{lab} > 80$ eV) and $\Theta = 165°$ ($\theta = 5°$). To obtain information regarding the electronic excitation process, the potential parameters in Eq. (4) for the excited $N_2(A^3\Sigma)$ state were evaluated using the optical data [30,31]. The potential parameters of $V_{C2}(r_3,\ A^3\Sigma)$ are listed in Table II(a). Since the electronic transition (electron promotion) time t_{el} (∼ a range of attosecond) in the intramolecular system is much shorter than the vibrational period t_{vib} (∼ 10 fs) of the N_2 molecule and the effective collision time t_{col} (∼ 5 fs) for the collision energies in this study, we assumed here the vertical electronic transition around an intramolecular distance of $r_3 = 1.24 \times 10^{-10}$ m [Fig. 11(b)]. The vibrational-energy scale in the figure was evaluated by referring to the potential curves for $N_2(X^1\Sigma)$, and $N_2(A^3\Sigma)$ determined above and the potentials by Gilmore (1965) [31]. It indicates feasible vibrational energy levels for the vertical electronic transition of $X^1\Sigma$ ($v = 0$) → $X^1\Sigma$ ($v \geqslant 3$) → $A^3\Sigma$ ($v' = 0$), where v and v' provide vibrational quantum numbers [see Fig. 11(b) as well]. The vibrational level in the $N_2(A^3\Sigma)$ state was assigned to be $v' = 0$ because of the experimental result of $\Delta E = Q = 6.2$ eV at lower collision energies of $E_{lab} < 90$ eV (Fig. 3). The energy transfer spectra in the narrow range of reduced energy transfer $\Delta E < 2.6$ eV are shown in Fig. 8(b). The prominent peak P_X in the raw CT spectrum is located around $\Delta E = 1.0$ eV. This is almost equal to the middle energy of the vibrational $v = 3$ and 4 levels. The peak P_X in the raw spectrum is discussed in Sec. V B.

V. DISCUSSION

A. Rotational excitations

Rotational excitations in lower-energy molecular collisions are explained using a hard-shell model [20–22]. Specific structures in the experimental energy transfer spectra for moderate energy Li^+-N_2 and Na^+-N_2 can be reproduced using a hard-shell model [16,38,39]. Figure 9(a) shows the energy transfer spectra evaluated by CT rigid-rotor and hard-shell model calculations for the Cs^+-N_2 collisions at $E = 8.8$ eV ($E_{lab} = 50$ eV) and $\Theta = 165°$. The spectrum obtained from the rigid-rotor model calculation has a sharp peak at approximately $\Delta E/E = 0$. The spectrum obtained using the hard-shell model (dotted curve) exhibits a maximum at a large energy transfer $\Delta E/E$ of approximately 0.85. In this model, the hard shell was approximated using an equipotential surface with distance $R(\gamma)$ depending on the orientation γ. Here the potential surface is defined by the height $V_{IM}(R_0)$ (= 8.67 eV) at the distance R_0 of the turning point in the

collisions [16]. The impact parameter for this treatment is a small value of $b = 0.22 \times 10^{-10}$ m. Therefore, it may be crucial to convert the angular momentum during backward scattering. Here, as an estimate, the maximum rotational angular momentum J_r was assumed to be determined by the total angular momentum in the collision system $L = b\mu v_0$, where b, μ, and v_0 are the impact parameter, reduced mass of the collision system, and initial projectile velocity, respectively. Consequently, the maximum rotational energy [rotational cutoff energy (RC)] was evaluated as $(\Delta E/E)_{RC} = B_e(2\pi L/h)^2/E$, where B_e and h are the rotational and Planck's constants, respectively. For the impact parameter $b = 0.22 \times 10^{-10}$ m, we obtained a cutoff energy of $(\Delta E/E)_{RC} = 0.13$. The dashed curve in Fig. 9(a) shows the energy-transfer spectrum obtained using the revised hard-shell model. However, the revised model still provided a significantly higher energy transfer.

The rotational excitation mechanisms in impulsive molecular collisions are understood effectively using the molecular orientation γ_0 defined at the turning point in the collisions [16,38]. The molecular orientation γ_0 dependences of the intensity defined by $I(\gamma_0) = d^2\sigma(\Theta, \Delta E/E, \gamma_0)/(d\Delta E/E d\gamma_0)$ were evaluated by CT rigid-rotor model calculations to determine the origin of the sharp peak in the spectrum around $\Delta E/E = 0$. Figure 9(b) shows the intensity $I(\gamma_0)$ at an energy transfer of $0 < \Delta E/E < 0.01$, which corresponds to the sharp peak position in the spectrum shown in Fig. 9(a). The prominent peak of $I(\gamma_0)$ is located at $\gamma_0 = 89°$. [An additional analysis at $\Theta = 150°$ revealed that the intensity $I(\Delta E/E)$ broadened slightly around $\Delta E/E = 0$. However, $I(\gamma_0)$ was almost identical to that in Fig. 9(b). Meanwhile, at $\Theta = 179°$ ($\pm 1°$), the prominent peak of $I(\gamma_0)$ was located around $\gamma_0 = 90°$.] This dramatic phenomenon can be attributed to the multiple-collision effect discussed by Buck *et al.* [40]. Lighter target molecules rotate to the molecular orientation with the lower energy $V_{IM}(R, \gamma)$ during collisions. At $\gamma = 90°$, the potential $V_{IM}(R,\gamma)$ has the lowest value, as illustrated in Table I.

The final rotational excitation energy in the backward scattering of Cs^+ ions from the N_2 molecules was significantly small, as discussed above. Therefore, the energy (momentum) transfers in the spectra calculated by the CT vibrating-rotor model shown in Figs. 7 and 8 were exclusively owing to the vibrational excitations of the N_2 molecules. The molecular-orientation-dependent intensities, $I(\gamma_0)$, were also evaluated for the energy transfer spectra calculated using the vibrating-rotor model at $E \leqslant 18.3$ eV ($E_{lab} \leqslant 105$ eV) and $\Theta = 165°$. The results indicate that the prominent peak in $I(\gamma_0)$ at the vibrational energy transfer $0 < \Delta E/E < 0.1$ was located around $\gamma_0 = 89°$, similar to $I(\gamma_0)$ in the rigid-rotor model calculations around $\Delta E/E = 0$. This was owing to the multiple collision effect in the vibrotational excitation processes, similar to rotational excitations. In this study, vibrotational excitations were calculated using the CT method with a vibrating-rotor model. However, evaluations using the classical sudden model [41] should also be useful for discussing momentum transfers in backward scattering.

The electronic excitation signal Z_1 observed in the experimental energy transfer spectra for the Cs^+-N_2 collisions can be attributed to the electronic excitation from the $N_2(X^1\Sigma)$ state to the $N_2(A^3\Sigma)$ state. Z_1 has narrow peak structure in the spectra, as shown in Fig. 8(a). This indicates that electronic transition occurred at a limited range of molecular orientations γ_0. Thereafter, we analyzed the experimental DCS and energy transfer spectra for the electronic excitations by assuming an electronic transition accompanied by the vibrational excitations around the orientation $\gamma_0 = 90°$.

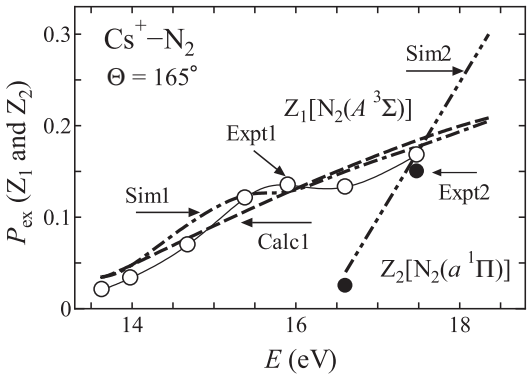

FIG. 10. Collision energy dependences of excitation probabilities P_{ex} for electronic transitions into the $N_2(A^3\Sigma)$ and $N_2(a^1\Pi)$ states at $\Theta = 165°$ ($\theta = 5°$). The open and filled circles connected with thin curves (Expt1 and Expt2) show the experimental P_{ex} evaluated from the excitation signals $Z_1(A^3\Sigma)$ and Z_2 ($a^1\Pi$), respectively, in the energy transfer spectra. The dashed curve (Calc1) shows the $P_{ex}(Z_1)$ evaluated by assuming the electronic LZ transition at a potential crossing between two interacting states. The dot-dashed curve (Sim1) shows $P_{ex}(Z_1)$ evaluated from the spectra calculated using a CT vibrating-rotor model (Fig. 13). The two-dot-dashed curve (Sim2) shows the $P_{ex}(Z_2)$ evaluated by simulation procedures of the signal Z_2 in the energy transfer spectra [Fig. 13(b)].

B. Electronic excitations accompanied by vibrational excitations

1. Excitation mechanisms

(a) Experimental excitation probability. Referring to the spectra calculated by the CT vibrating-rotor model (Fig. 8), the collision energy E dependence of the excitation probability $P_{ex}(A^3\Sigma)$ for the $N_2(X^1\Sigma) \rightarrow N_2(A^3\Sigma)$ transition with excitation energy $Q = 6.2$ eV at $\Theta = 165°$ ($\theta = 5°$) was deduced by evaluating the intensity I_{Z1} of Z_1 and total intensity I_T, i.e., $P_{ex} = I_{Z1}/I_T$. At a higher energy of $E = 18.3$ eV ($E_{lab} = 105$ eV), Z_1 and Z_2 were almost combined (Fig. 2), and the intensities I_{Z1} were evaluated at $E \leqslant 17.5$ eV ($E_{lab} \leqslant 100$ eV). The open circles connected to the thin curve in Fig. 10 indicate the experimental excitation probability $P_{ex}(Z_1)$.

The transition probability p through the spin-orbit coupling interaction at a potential crossing can be represented by the Landau-Zener (LZ) formula [23], similar to that for radial coupling [6]. Assuming LZ transitions through the potential crossing, the potential for the excited state and the potential parameters at the crossing were evaluated using the fitting procedure of the probability $P_{ex}(Z_1)$ in Fig. 10 to obtain rudimentary information on the electronic excitation. The electronic transition presumably occurred at the molecular orientation $\gamma = \pi/2$ under the collisional conditions discussed above. The fitting procedure was conducted using the potentials $V_{IM}(R,\ \gamma = \pi/2)$ and $V_{IM}(R)$ listed in Table I,

and the adjustable potential V_{IM} $(R, \gamma = \pi/2)^*$ for the excited $Cs^+ + N_2(A^3\Sigma)$ state. The excitation probability was evaluated using the relation $P_{ex} = \sigma(\Theta)_{ex}/\sigma(\Theta)$, where $\sigma(\Theta)_{ex}$ is the excitation DCS calculated considering the electronic transition between the potentials of $V_{IM}(R, \gamma = \pi/2)$ and V_{IM} $(R, \gamma = \pi/2)^*$. $\sigma(\Theta)$ is the total DCS calculated using the spherical potential $V_{IM}(R)$. The excited-state potential function V_{IM} $(R, \gamma = \pi/2)$, excitation energy Q, intermolecular potential crossing distance R_C, potential height $V(R_C)$ at R_C, and coupling energy H_{12} at the crossing deduced through the DCS calculations are summarized in Table II(b). The deduced transition parameter $\Gamma_{12} = (H_{12})^2/\Delta F_{12}$ determining the transition probability was 1.0×10^{-12} eV m, where ΔF_{12} is the difference in slope between the potentials V_{IM1} and V_{IM2} around the potential $V(R_C) = 13.35$ eV. The small transition parameter $\Gamma_{12} = 1.0 \times 10^{-12}$ eV m is almost identical to those for the quasisymmetric Li^+–He, Na^+–Ne, and K^+–Ar systems studied experimentally [8,10,11]. The dashed curve (Calc1) in Fig. 10 denotes the excitation probability calculated using the potential parameters determined through the fitting procedure. Thus, the calculations reproduced the experimental results satisfactorily.

A significant electronic excitation into the $Cs^+ + N_2(a^1\Pi)$ state was also observed at collision energies of $E \geqslant 16.6$ eV ($E_{lab} \geqslant 95$ eV), i.e., the signal Z_2 in the energy transfer spectra shown in Fig. 2. The excitation probabilities $P_{ex}(a^1\Pi)$ for Z_2 evaluated approximately from the experimental spectra at $E = 16.6$ and 17.5 eV ($E_{lab} = 95$ and 100 eV) are denoted by the filled circles in Fig. 10. The potential crossing parameters and excited-state potential at the molecular orientation $\gamma = \pi/2$ estimated using the experimental data are listed in Table II(b). The excited-state potential $V_{IM}(R, \gamma)^*$ of the excited $Cs^+ + N_2(a^1\Pi)$ state are composed of the interatomic potential $V_{IA}(r)^* = 3080\exp(-3.85r)$ eV of the imaginary Cs^+–N* system. The potential height $V_{IM}(R_C,) = 16.4$ eV for the $Cs^+ + N_2(a^1\Pi)$ state shown in the table is nearly equal to $V_{IM}(R_C) \sim 15$ eV evaluated for the K^+–N_2 collisions [14].

(b) Electronic excitations through momentum transfer. As described in Sec. IV B, the electronic excitation process was analyzed by evaluating the momentum transfer in Cs^+–N_2 collisions. Figure 8(b) shows the energy transfer spectra in a narrow range of $\Delta E < 2.6$ eV calculated at $E = 14.7$ eV ($E_{lab} = 84$ eV) and $\Theta = 165°$. The energy $E = 14.7$ eV is slightly higher than the potential height of $V_{IM}(R_C) = 13.4$ eV at the crossing distance R_C for the $N_2(A^3\Sigma)$ excitation. The prominent peak P_X in the figure is located around the energy transfer of $\Delta E = 1.0$ eV. This is almost in the middle of the vibrational energy levels of $v = 3$ and 4. For vertical electronic transition between the $N_2(X^1\Sigma)$ and $N_2(A^3\Sigma)$ states, the feasible transition path is given by $X\,^1\Sigma(v=0) \rightarrow X\,^1\Sigma(v \geqslant 3) \rightarrow A^3\Sigma(v' = 0)$ at the intramolecular distance $r_3 = 1.24 \times 10^{-10}$ m [Fig. 11(b)]. Therefore, the vibrational number $v = 3$ is the lowest intermediate energy level for the electronic transitions. At $E = 14.0$ eV ($E_{lab} = 80$ eV) and $\Theta = 165°$, the peak P_X is located at $\Delta E \sim 0.81$ eV. This is almost identical to the vibrational energy level of $\Delta E = 0.85$ eV for $v = 3$. The collision energy $E = 14.0$ eV was nearly equal to the threshold energy of $E_{th} \sim V_{IM}(R_C)$ (= 13.4 eV) for electronic excitation. Thus, the peak Px is closely related to the electronic excitation process.

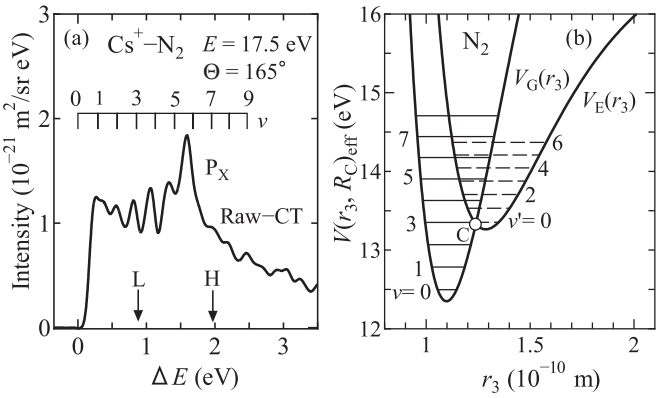

FIG. 11. (a) Raw energy transfer spectrum in the CM system evaluated through CT vibrating-rotor model calculation at $E = 17.5$ eV ($E_{lab} = 100$ eV) and $\Theta = 165°$. The arrows L and H indicate the energy positions to evaluate the electronic excitation probability $P_{ex}(A^3\Sigma)$ from the energy transfer spectrum. The energy scale v indicates the vibrational energy levels $v = 0$–9 for the ground $N_2(X^1\Sigma)$ state. (b) Intramolecular potential crossing model between the $N_2(X^1\Sigma)$ (V_G) and $N_2(A^3\Sigma)$ (V_E) states for Cs^+–N_2 system. At the potential crossing C, the distance is $r_{3C} = 1.24 \times 10^{-10}$ m, effective potential height $W(r_{3C})_{eff} = V_{IM}(R_C) = 13.35$ eV, and molecular orientation $\gamma = \pi/2$.

An analysis of the classical trajectories included at $\Delta E < 1.5$ eV in Fig. 8(b) of $E = 14.7$ eV indicated that the energy transfers depend directly on the initial vibrational phase η. This is because the classical trajectories for each phase η have different onset energies. P_X appears around the phases of $\eta_m = 0.15\pi$ and 1.65π, which provide the largest onset energy $(\Delta E/E)_{on}$, as shown in Fig. 7(b). Thus, P_X is attributed to a type of pseudo-rainbow effect in the vibrational initial phase η. The phases η_m depend on the collision energies, e.g., $\eta_m = 0.7\pi$ and 1.2π for $E = 8.8$ eV shown in Fig. 7.

Figure 11(a) shows the energy transfer spectrum in the range of $\Delta E < 3.5$ eV, calculated at $E = 17.5$ eV ($E_{lab} = 100$ eV) and $\Theta = 165°$. The spectrum for this higher collision energy exhibited no signal around $\Delta E = 0$ and had an onset energy $\Delta E = 0.10$ eV. The prominent (pseudo-rainbow) peak P_X for this higher energy was located around $\Delta E = 1.6$ eV, which was the middle energy for the levels $v = 5$ and 6. The location $\Delta E(P_X) = 1.6$ eV was higher than $\Delta E(P_X) = 1.0$ eV at $E = 14.7$ eV. The P_X locations were considered to explain the collision energy dependences of $\Delta E(Z_1)$ shown in Fig. 3 and $P_{ex}(A^3\Sigma)$ in Fig. 10. These features of the calculated spectra were interpreted using the intramolecular potential crossing [42] shown in Fig. 11(b). This figure shows the crossing between the effective potentials $V_G(X\,^1\Sigma)$ and $V_E(A^3\Sigma)$ for the electronic ground $N_2(X^1\Sigma)$ and excited $N_2(A^3\Sigma)$ states. In this crossing model, the energy level $v = 3$ of $V_G(r_3)$ coincides (crosses) with the energy level $v' = 0$ of $V_E(r_3)$ at a distance of $r_{3C1} = 1.24 \times 10^{-10}$ m. The intramolecular crossing distance r_{3C1} is also indicated in Table II(a). The potential height of $V_{G,E}(r_{3C})$ at the crossing point C was assumed to be equivalent to the experimental intermolecular potential of $V_{IM}(R_C) = 13.35$ eV at the distance R_C. Consequently, the potentials $V_G(r_3)$ and $V_E(r_3)$ in the figure are given by $V_G = V_{C1}(r_3, X^1\Sigma) + 12.35$ eV and

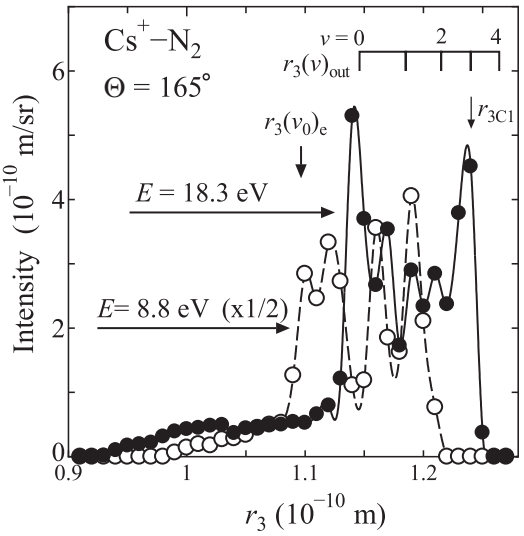

FIG. 12. Intramolecular distance r_3 spectrum at collision energy $E = 8.8$ and 18.3 eV ($E_{\rm lab} = 50$ and 105 eV) and scattering angle $\Theta = 165°$. The distance r_3 is defined at the turning point in the collisions, and the resolution width is $\Delta r_3 = 0.01 \times 10^{-10}$ m. The open circles with dashed curves and filled circles connected with solid curves show the spectra at $E = 8.8$ eV and 18.3 eV, respectively. The arrow $r_3(v_0)_e$ shows the equilibrium molecular distance ($r_3 = 1.098 \times 10^{-10}$ m) of the ground electronic $X^1\Sigma(v = 0)$ state. The scale $r_3(v)_{\rm out}$ indicates the outermost r_3 distance for each vibrational state v. Furthermore, the arrow r_{3C1} indicates the crossing distance between the potentials of the levels $v = 3$ for the $N_2(X^1\Sigma)$ state and $v' = 0$ for the $N_2(A^3\Sigma)$ state shown in Fig. 11(b).

$V_E = V_{C2}(r_3,\ A^3\Sigma) + 7.04$ eV, respectively, from the potentials $V_{C1}(r_3,\ X^1\Sigma)$ and $V_{C2}(r_3,\ A^3\Sigma)$ evaluated above. The intramolecular crossing corresponds to that between the interaction potentials $W(r_1, r_2, r_3)$ given by Eq. (3) for the ground $Cs^+ + N_2(X^1\Sigma)$ and excited $Cs^+ + N_2(A^3\Sigma)$ states at R_C and the orientation $\gamma = \pi/2$, assuming a vertical electronic transition [13].

The $N_2(A^3\Sigma)$ excitation was assumed here to proceed through the intramolecular crossing at $r_{3C1} = 1.24 \times 10^{-10}$ m shown in Fig. 11(b). To evaluate the assumption, we analyzed the intramolecular distance r_3 at the turning points in the collisions. In our case, the turning point distance R_0 was close to the potential crossing R_C. This was because the collision energies E studied here are nearly equal to the threshold collision energy of $E_{\rm th} \sim V_{\rm IM}(R_C)$ (= 13.35 eV). Figure 12 shows the distributions of the distances r_3 at collision energies $E = 8.8$ and 18.3 eV and scattering angle $\Theta = 165°$. $E = 18.3$ eV is the highest energy for our detailed study. As is evident in the figure, the vibrational excitation to $r_3 > 1.21 \times 10^{-10}$ m can be observed at $E > 8.8$ eV ($E_{\rm lab} > 50$ eV). $r_3 = 1.24 \times 10^{-10}$ m at $v = 3$ corresponds to the intramolecular crossing distance r_{3C1} between the potential curves of the $X\ ^1\Sigma$ and $A^3\Sigma$ states. This is likely to be the reason that the $N_2(A^3\Sigma)$ excitation was observed significantly in the collisions at energies $14 < E < 18$ eV and angle $\Theta = 165°$. The r_3 distributions at the turning points in the L^+-N_2 and K^+-N_2 collisions were also analyzed around the threshold angle $\theta_{\rm th}(\Theta_{\rm th} < \Theta_C)$, where the electronic excitations of the N_2 molecules were observed as mentioned above [13,14]. For these systems, the intramolecular distances were located at $r_3 < 1.2 \times 10^{-10}$ m. This is smaller than the crossing distance $r_{3C1} = 1.24 \times 10^{-10}$ m for the $N_2(A^3\Sigma)$ excitation. Thus, the vibrational excitations in the Cs^+-N_2 collisions near the threshold energy $E_{\rm th}$ differ significantly from those in the Li^+-N_2 and K^+-N_2 collisions. Accordingly, the electronic excitation around the angles $\theta_{\rm th}$ in these lighter systems is considered to occur through the vertical electronic transition around the intramolecular equilibrium distance $r_3 \sim 1.1 \times 10^{-10}$ m [13].

In the Cs^+-N_2 collisions at higher energy of $E = 17.5$ eV ($E_{\rm lab} = 100$ eV), another $N_2(a^1\Pi)$ excitation was observed with an observably high probability. Therefore, the experimental spectrum can be reproduced considering both transitions to the $N_2(A^3\Sigma)$ and $N_2(a^1\Pi)$ states. In the vertical electronic transition $N_2(X^1\Sigma) \rightarrow N_2(a^1\Pi)$, the intramolecular potential crossing was evaluated to be located at $r_{3C2} = 1.18 \times 10^{-10}$ m between the vibrational level v = 1 for $N_2(X^1\Sigma)$ and v′ = 0 for $N_2(a^1\Pi)$. Therefore, the feasible initial vibrational levels are primarily owing to $1 \leqslant v < 3$ for excitation to the $N_2(a^1\Pi)$ state, considering the $N_2(A^3\Sigma)$ excitation occurring at $v \geqslant 3$ [Fig. 11(a)]. The intramolecular potential parameters for the excited-state potential $V_{C3}(r_3,\ a^1\Pi)$ of the $N_2(a^1\Pi)$ state are also given in Table II(a).

(c) Simulations of energy transfer spectra with electronic excitations. Figure 13(a) shows the energy transfer spectra calculated by CT vibrating-rotor model and obtained experimentally at the CM energy $E = 14.7$ eV ($E_{\rm lab} = 84$ eV) and an angle $\Theta = 165°$. The CT calculations were performed considering the electronic transition $N_2(X^1\Sigma) \rightarrow N_2(A^3\Sigma)$ ($Q = 6.2$ eV). The signals around the dominant peak P_X in the raw CT spectrum at energies of $\Delta E_L - \Delta E_H$ shown in Fig. 8(b) were promoted to the signal $P_{X'}$ located at $\Delta E\ (= Q) = 6.2$ eV in the dashed curve, where ΔE_L corresponds to the vibrational energy for the $v = 3$ level. Meanwhile, ΔE_H is arbitrarily assumed to correspond to the excitation energy yielding half the peak height of P_X. The transition was also assumed to occur for trajectories with molecular orientations of $88 < \gamma < 90°$ ($\Delta\gamma = \pm 1°$), according to the discussion in Sec. V A. The calculation reasonably reproduces the experimental Z_1 peak and the distinct shallow minimum in the experimental spectrum around $\Delta E = 1.2$ eV (the arrow SM in the figure) as an inclining structure around the arrow INC in the figure.

Figure 13(b) shows the experimental and simulated energy transfer spectra at $E = 17.5$ eV and $\Theta = 165°$. In the raw CT spectrum, the peak $P_{X'}$ for Z_1 mostly originates from the peak P_X mentioned above [Fig. 11(a)]. In contrast, the peak $P_{Y'}$ for Z_2 is mostly given by the signals at the vibrational level $v < 3$ shown in Fig. 11(a). The peak was finally determined through curve fitting by adjusting the correction factor F of the peak height, orientation width $\Delta\gamma$, and energy width $\Delta(\Delta E)$ to reproduce the tail intensity at the large energy transfers of $\Delta E = 9.5$–11.5 eV. The simulated spectrum with the excitation energies of $\Delta E_{Z1} = 7.0$ eV [$\Delta\varepsilon_{Z1} (= \Delta E_{Z1} - Q_{Z1}) = 0.8$ eV] and $\Delta E_{Z2} = 9.0$ eV ($\Delta\varepsilon_{Z2} = 0.5$ eV) effectively reproduces the experiment (Fig. 3). The correction factors evaluated through the simulations were $F = 0.4$, 0.8, and 1.0 at $E = 16.6$, 17.5, and 18.3 eV ($E_{\rm lab} = 95$, 100, and 105 eV), respectively [Moreover, $F < 0.05$ at $E = 15.9$ eV ($E_{\rm lab} = 91$ eV)].

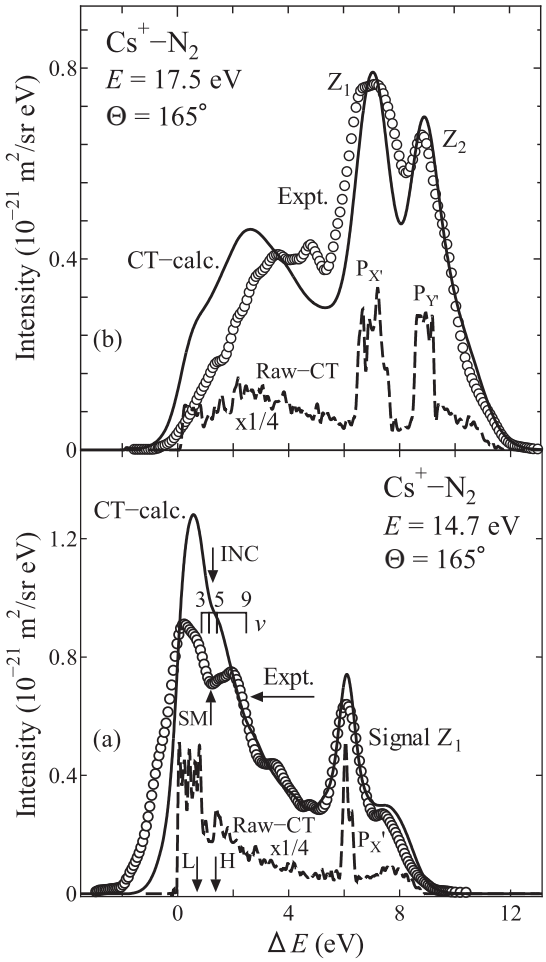

FIG. 13. Energy-transfer spectra in the CM system simulated through CT vibrating-rotor model calculations. The solid and dashed curves show the convoluted and raw CT spectra, respectively. The raw calculations decrease by a factor of 1/4. The open circles show the experimental spectra for comparison. (a) Spectra at $E = 14.7$ eV ($E_{\rm lab} = 84$ eV) and $\Theta = 165°$ revised from Fig. 8(a) by considering the electronic transition into the $N_2(A^3\Sigma)$ state. The peak $P_{X'}$ in the raw CT spectrum represents the excitation signal Z_1 in the experimental and convoluted CT spectra. The arrow SM indicates a shallow minimum position in the experimental DCS, and the arrow INC indicates an inclining structure position in the convoluted CT spectrum. (b) Spectra at $E = 17.5$ eV ($E_{\rm lab} = 100$ eV) and $\Theta = 165°$ simulated considering electronic transitions to the $N_2(A^3\Sigma)$ (signal Z_1) and $N_2(a^1\Pi)$ (signal Z_2) states. The peaks $P_{X'}$ and $P_{Y'}$ in the raw CT spectrum represent the excitation signals Z_1 and Z_2, respectively.

The excitation probabilities $P_{\rm ex}$ [$= S_{PX'}(S_{PY'})/S_{\rm total}$] for the electronic transitions of $X\,^1\Sigma \rightarrow A^3\Sigma$ and $a^1\Pi$ were deduced by evaluating the integrated intensities $S_{PX'}$ and $S_{PY'}$ of the raw excitation signals $P_{X'}$ and $P_{Y'}$[Figs. 13(a) and 13(b)], and $S_{\rm total}$ of the total raw CT signals. The dot-dashed (Sim1) and two-dot-dashed (Sim2) curves in Fig. 10 show the energy dependences of the probabilities $P_{\rm ex}$ for $N_2(A^3\Sigma)$ and $N_2(a^1\Pi)$ excitations, respectively, evaluated using the spectra simulated by the CT vibrating-rotor model. The calculations effectively reproduced the experimental energy dependence. As shown in Fig 10, the probability $P_{\rm ex}$ (Z_2) for the $N_2(a^1\Pi)$ excitation increased abruptly as the collision energy increased. This indicates that the excitation probability was primarily determined by the $P_{\rm ex}$ ($a^1\Pi$) at energies $E > 17.5$ eV ($E_{\rm lab} > 100$ eV). The probability was estimated to be $P_{\rm ex}(a^1\Pi) = 1$ at the higher energies of $E > 26$ eV ($E_{\rm lab} > 150$ eV).

The energy transfer spectrum in the laboratory system at high-energy $E_{\rm lab} = 250$ eV ($E = 43.6$ eV) and angle $\theta = 5°$ was calculated using the CT vibrating-rotor model to interpret the specific experimental spectrum. The solid curve in Fig. 4 shows the simulated energy-transfer spectra at $E_{\rm lab} = 250$ eV and $\theta = 5°$. The simulated spectrum (solid curve) was obtained using the intramolecular potential $V_C(r_3, a^1\Pi)$ for the excited $N_2(a^1\Pi)$ state with the excitation energy $Q = 8.5$ eV [listed in Table II(a)] under the assumption that $P_{\rm ex}(a^1\Pi) = 1$. In the simulation, the potential $V_{\rm IM}(R, \gamma)^*$ for the excited $Cs^+ + N_2(a^1\Pi)$ state was evaluated using the interatomic function $V_{\rm IA}(r)^* = 3080\exp(-3.85r)\,eV$, as determined above. For comparison, the dotted curve in the figure shows the spectrum calculated for the ground-state potential $V_C[r_3, N_2(X^1\Sigma)]$ with $Q = 0$. Thus, the pseudo-rainbow structure observed in the experimental spectrum at large collision energy was reproduced effectively through simulation under the assumption of $N_2(a^1\Pi)$ excitation with $P_{\rm ex}(a^1\Pi) = 1$. Additionally, refined CT calculations using the vibrating-rotor model considering potential surface crossing [13] and intramolecular crossing would provide more detailed information on the electronic excitation processes.

2. *Charge-overlap model potentials*

In the ion-molecule (and -atom) collisions, charge exchange reactions were generally observed with high probabilities as well as direct particle excitations [7,13]. However, only the excitations of the N_2 molecules (rather than the charge exchange reaction) were observed in the Cs^+−N_2 collisions. To understand the experimental results, the diabatic intermolecular potentials at the molecular orientation $\gamma = \pi/2$ for the ground $Cs^+ + N_2$ state, charge-transferred Cs(6s) $+ N_2^+$ state, and two electronically excited $Cs^+ + N_2(A^3\Sigma$ and $(a^1\Pi)$ states were evaluated using the empirical charge-overlap model [10]. The model was applied successfully to discuss the excitation processes in atomic collisions between the closed-shell particles A and B. Therefore, the excited-state potential of A + B*, where B* is in an excited state, could be evaluated approximately by the overlap of the charge densities between the particles A and B^+, omitting the promoted outer electron of particle B* [43]. For the excited $N_2(A^3\Sigma)$ and $N_2(a^1\Pi)$ molecules, the electrons in the molecular orbital $1\pi_u$ and $3\sigma_g$, respectively, are promoted to the outer $1\pi_g$ orbital. Furthermore, the intermolecular potentials $V_{\rm IM}(R,\ \gamma = \pi/2)$ for Cs^+ ion excitations to $Cs^{+}* + N_2$, and $Cs^{2+} + N_2^-$ states were calculated using the empirical model to obtain information on the spin-changing electronic transition [$N_2(X^1\Sigma)$ state $\rightarrow N_2(A^3\Sigma)$ state].

(a) Charge transfer and N_2 *excitations*. The ground-state Cs^+ –N_2 potential was evaluated using the overlap of charge densities $\rho_{i,j}$ between the $Cs^+(5p^6)$ ion and $N(2p^3)$ atom [36], similar to the statistical model calculations in Sec. III. The potential for the charge transferred Cs + N_2^+ state ($Q =$ 11.7 eV) was evaluated using the potential of the imaginary

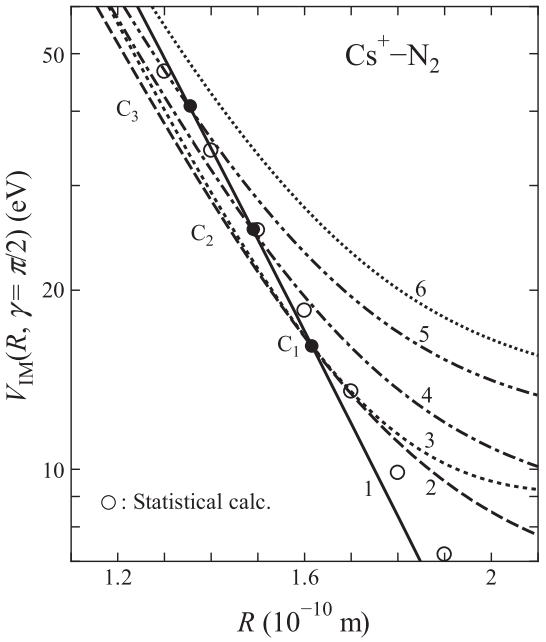

FIG. 14. Diabatic potentials at molecular orientation $\gamma = \pi/2$ for the ground and excited electronic states evaluated using the charge-overlap model by Ref. [10]. The electronic states of model potential curves at the separated distances are as follows: (1) $Cs^+ + N_2(X^1\Sigma)$, (2) $Cs^+ + N_2(A^3\Sigma)$ ($Q = 6.2$ eV), (3) $Cs^{2+} + N_2^-$ ($Q_{\rm eff} = 21.0$ eV), (4) $Cs^+ + N_2(a^1\Pi)$ ($Q = 8.5$ eV), (5) Cs(6s) + $N_2^+(X\,^2\Sigma)$ ($Q = 11.7$ eV), and (6) Cs^+*$(5p^56s) + N_2(X^1\Sigma)$ ($Q = 13.4$ eV). The open circles show the statistical ground-state potential for comparison. The filled circles C_1–C_3 indicate the potential crossing positions.

Cs(6s)–N*$(2s^22p^{2.5})$ system, considering the total number of electrons $n = 13$ for the N_2^+ ion. The $N_2(A^3\Sigma)$ and $N_2(a^1\Pi)$ molecules were considered as N_2^+ ions based on the analogy of atomic collision systems to evaluate the potentials of the electronically excited $Cs^+ + N_2(A^3\Sigma)$ and $Cs^+ + N_2(a^1\Pi)$ states. Herein, the intermolecular potentials were determined using the spectroscopic data of the equilibrium N-N distance r_e and excitation energies Q. Figure 14 shows the calculated model potentials at the molecular orientation $\gamma = \pi/2$. Ground-state potential curve 1 agrees well with that evaluated using the statistical model shown by the open circles in the figure. Excited-state curves 2, 4, and 5 cross curve 1 at points C_1–C_3 shown by the filled circles. The potential parameters of the crossings C_1 and C_2 listed in Table II(b) agree reasonably with the experimental values. The crossing C_3 is located at $R_{C3} = 1.36 \times 10^{-10}$ m and $V_{IM}(R_{C3}) = 40$ eV. The potential height $V_{IM}(R_{C3}) = 40$ eV is observably higher than the experimental $V_{IM}(R_{C1}) = 13.4$ eV and $V(R_{C2}) = 16.4$ eV. This is likely to be reason that the charge exchange reaction was not observed in this study. The model potential for the Li^+–N_2 system calculated additionally also reproduces the potential crossing for the excited $Li^+ + N_2(a^1\Pi)$ state evaluated by *ab initio* calculations and experiments [13].

(b) Cs^+ *excitation and ion-pair formation*. The potential $V_{IM}(R, \gamma = \pi/2)$ for the excited Cs^+*$(5p^56s) + N_2$ state was evaluated by calculating the potential for the Cs^+*–N system using the charge overlap model. Curve 6 in Fig. 14 shows the potential for the $Cs^{+*}(5p^56s) + N_2$ state ($Q = 13.35$ eV), which crosses potential curve 1 at a higher potential $V_{IM}(R_C, \gamma = \pi/2)$ of approximately 120 eV. Therefore, the spin-change process cannot be interpreted by considering this excitation process.

The potential for ion-pair formation in the $Cs^{2+} + N_2^-$ state was calculated as a final attempt. The electronic ion-pair configuration of $Li^- + He^{2+}$ was reported in the *ab initio* potential energy calculation for the Li^+–He system, which was identified down to a shorter distance of $R = 0.25 \times 10^{-10}$ m [8]. Similarly, the electronic excitation processes in K–N_2 and –CO collisions were discussed considering the ion-pair formation of the $K^+ + N_2^-$ and CO^- states [44]. The intermolecular potential of the $Cs^{2+} + N_2^-$ state was calculated by assuming the relation of $V_{IM}(R, \gamma = \pi/2) = V_{OV}(R, \gamma = \pi/2) + V_{Coul}(R) + Q_{eff}$, where $V_{OV}(R, \gamma = \pi/2)$ is the intermolecular potential for the $Cs^{2+} + N_2$ system given by the charge overlap model, and $V_{Coul}(R)$ is the Coulombic potential between the positive charge ($z_i = 2$) on the Cs^{2+} ion and the additional negative charge density $-\rho_e$ on the N_2^- ion (total charge $z_e = -1$) [45]. The charge density ρ_e was evaluated using the normalized radial wave function of the s-type orbital $R_{WF}(r) = Ar^n \exp(-\alpha r)$ centered at the center of gravity of the N_2 molecule. The intramolecular equilibrium distance for the N_2^- molecule was assumed to be $r_e \sim 1.1 \times 10^{-10}$ m, which is equal to that of the ground-state N_2 molecule. Curve 3 in Fig. 14 shows the potential for the $Cs^{2+} + N_2^-$ state fitted at the crossing C_1 in the figure between curves 1 and 2 [$V_{IM}(R_{C1}) = 16$ eV] by adjusting the orbital function R_{WF} and effective excitation energy Q_{eff}. The result was obtained using $n = 2$ and $\alpha = 4.7 \times 10^{10}\,\mathrm{m}^{-1}$, which yields the maximum radius of the charge density ρ_e of $r_{max} = 0.4 \times 10^{-10}$ m. The effective excitation energy was $Q_{eff} = 21.0$ eV. This is moderately lower than the ionization energy $IP = 25.1$ eV of the Cs^+ ions. The Coulombic potential is given by $V_{Coul}(R) = -28.8 \times 10^{-10}/R$(eV) at $R > 1.0 \times 10^{-10}$ m.

(c) Spin-changing electronic transition. As discussed above, the spin-changing reaction occurs through the two-step process of $Cs^+ + N_2(X^1\Sigma) \rightarrow Cs^{2+} + N_2^- \rightarrow Cs^+ + N_2(A^3\Sigma)$. Total spins of the initial $Cs^+ + N_2(X^1\Sigma)$ and final $Cs^+ + N_2(A^3\Sigma)$ states are $S = 0$ and 1, respectively, whereas the total spins of intermediate $Cs^{2+} + N_2^-$ state are $S = 0$ and 1. First, an electronic transition occurs at the crossing C_1 in Fig. 14 between curves 1($Cs^+ + N_2$) and 3 ($Cs^{2+} + N_2^-$) through radial coupling [6]. The Cs^{2+} ion has doublet states of $Cs^{2+}(5p^5\,^2P_{3/2})$ and $Cs^{2+}(5p^5\,^2P_{1/2})$ with an energy difference $\Delta Q = 1.7$ eV. Second, during the Cs^{2+}–N_2^- collisions along curve 3 at $R < R_{C1}$, the initial total spin $S = 0$ of the intermediate system is modified to $S = 1$ owing to spin-orbit coupling [23,33] through the interaction between the quasimolecular $Cs^{2+}(^2P_{3/2}$ and $^2P_{1/2}) + N_2^-$ states [46]. Finally, at the second passage of C_1, the electronic transition from curve 3 ($Cs^{2+} + N_2^-, S = 1$) to curve 2[$Cs^+ + N_2(A^3\Sigma)$, $S = 1$] occurs via the radial coupling [6], involving electron exchange [47]. These processes result in a spin-changing $N_2(X^1\Sigma) \rightarrow N_2(A^3\Sigma)$ excitation. Thus, electronic $N_2(A^3\Sigma)$ excitation occurs at the second passage of C_1 following the transition to the $Cs^{2+} + N_2^-$ state at the first passage of C_1. Furthermore, the intramolecular potential $V_C(r_3)$ for N_2^- is estimated to be almost

equal to the ground-state potential for N_2 molecule. This is why the $N_2(A^3\Sigma)$ excitation can be interpreted reasonably considering the pseudo-rainbow effect on momentum transfer in Cs^+-N_2 collisions, as discussed in Sec. V B 1.

VI. CONCLUSION

The energy transfer processes in the Cs^+-N_2 collisions were studied experimentally at the laboratory collision energies of $E_{lab} = 50-250$ eV and scattering angles of $\theta > 2^\circ$ via differential scattering spectroscopy. The experimental results were analyzed using the classical trajectory (CT) calculation method. Specific electronic excitations to the $N_2(A^3\Sigma)$ and $N_2(a^1\Pi)$ states were observed with significant excitation probabilities P_{ex} in the backward scattering at lower CM energies $E = 13.6-18.3$ eV ($E_{lab} = 78-105$ eV) and a CM angle $\Theta = 165^\circ$ ($\theta = 5^\circ$). CT calculations using vibrating-rotor model indicated that the electronic transition to the $N_2(A^3\Sigma)$ state occurred mostly around the molecular orientation $\gamma_0 = \pi/2$ in the collisions and at vibrotational excitations $\Delta E/E < 0.12$.

By analyzing the E dependence of the experimental probabilities $P_{ex}(E)$ for the $N_2(A^3\Sigma)$ excitation, the intermolecular potential crossing for the orientation $\gamma = \pi/2$ was determined to be located at a distance of $R_C = 1.69 \times 10^{-10}$ m and a potential height of $V_{IM}(R_C) = 13.4$ eV. The experimental $P_{ex}(E)$ for the $N_2(a^1\Pi)$ excitation approximately provided $V_{IM}(R_C) = 16.4$ eV at $R_C = 1.62 \times 10^{-10}$ m. Furthermore, the probabilities P_{ex} for the $N_2(A^3\Sigma)$ and $N_2(a^1\Pi)$ excitations were evaluated by simulating the experimental energy transfer spectra. The simulations indicated that $N_2(A^3\Sigma)$ excitation was the dominant excitation process at lower energies of $E < 17.5$ eV ($E_{lab} < 100$ eV). The analyses, where the transitions into the $N_2(A^3\Sigma)$ and $N_2(a^1\Pi)$ states were assumed to occur primarily at vibrational levels $v \geqslant 3$ and $1 \leqslant v < 3$, respectively, were related to the crossings between the intramolecular potentials of the electronic ground and excited states.

Finally, the diabatic intermolecular potentials of the electronic ground and excited states were evaluated using an empirical charge overlap model. The evaluations effectively reproduced potential crossings between the ground and excited states, and reasonably interpreted the spin-changing excitation mechanism for the $N_2(X^1\Sigma) \rightarrow N_2(A^3\Sigma)$ transition.

In the impulsive Li^+-N_2 and K^+-N_2 collisions at small scattering angles studied earlier, vertical electronic transitions to the $N_2(a^1\Pi)$ and $N_2(a'^1\Sigma$ or $w^1\Delta)$ states, respectively, were observed to occur around the intramolecular equilibrium distance r_e. Meanwhile, no singlet-triplet transition was observed. These results differ from our results. There are two likely causes of this inconsistency. First, the Li^+-N_2 and K^+-N_2 systems have no coupling energy for the singlet-triplet transition, i.e., $H_{ij} = 0$. The other originates from the fact that the vibrational motion of the N_2 molecules during the Cs^+-N_2 collisions is considerably large and the intramolecular distance r_3 reaches to the crossing distance $r_{3C} = 1.24 \times 10^{-10}$ m in the backward scattering around the threshold collision energies.

ACKNOWLEDGMENTS

We gratefully acknowledge the recommendation of the late Emeritus Prof. H. Inouye (Tohoku University, Sendai, Japan) during the first stage of our serial studies. We are grateful to Emeritus Profs. Y. Sato (Tohoku University, Sendai, Japan) and N. Shimakura (Niigata University, Niigata, Japan) for their effective discussions. We gratefully acknowledge Emeritus Prof. H. Nakamura (Institute for Molecular Science, Okazaki, Japan) and Prof. F. Koike (Sophia University, Tokyo, Japan) for their discussions on spin-forbidden reactions. S.K. is grateful to the late Dr. A. Kohlhase (Munich, Germany) for the effective discussions regarding molecular collisions. We are grateful to Y. Shiraishi, K. Nishimura, G. Ogoh, and Y. Watanabe (Nagoya Institute of Technology, Nagoya, Japan) for their contributions to this study.

[1] J. C. Brenot, D. Dhuicq, J. P. Gauyacq, J. Pommier, V. Sidis, M. Barat, and E. Pollack, Phys. Rev. A **11**, 1245 (1975).
[2] D. C. Lorents and G. M. Conklin, J. Phys. B **5**, 950 (1972).
[3] V. V. Afrosimov, Y. S. Gordeev, and V. M. Lavrov, Zh. Exsp. Teor. Fiz. **68**, 1715 (1975) [Sov. Phys. JETP **41**, 860 (1976)].
[4] J. Ø. Olsen, T. Andersen, M. Barat, C. Courbin-Gaussorgues, V. Sidis, J. Pommier, J. Agusti, N. Andersen, and A. Russek, Phys. Rev. A **19**, 1457 (1979).
[5] A. Russek, Phys. Rev. A **4**, 1918 (1971).
[6] C. Zhu and H. Nakamura, J. Chem. Phys. **102**, 7448 (1995).
[7] S. Kita and N. Shimakura, Phys. Rev. A **55**, 3504 (1997).
[8] S. Kita, J. Itaya, Y. Sawatari, T. Tabata, T. Hayashi, N. Shimakura, and S. Koseki, J. Phys. Soc. Jpn **87**, 024302 (2018).
[9] M. Barat and W. Lichten, Phys. Rev. A **6**, 211 (1972).
[10] S. Kita and J. Itaya, J. Phys. Soc. Jpn **90**, 054301 (2021).
[11] S. Kita, H. Tanuma, and M. Izawa, J. Phys. B **20**, 3089 (1987).
[12] S. Kita, T. Hasegawa, H. Tanuma, and N. Shimakura, Phys. Rev. A **52**, 2070 (1995).
[13] S. Kita, H. Tanuma, I. Kusunoki, Y. Sato, and N. Shimakura, Phys. Rev. A **42**, 367 (1990).
[14] H. Inouye, K. Niurao, and Y. Sato, J. Chem. Phys. **64**, 1250 (1976), private communication (1990).
[15] E. J. Quintana and E. Pollack, Phys. Rev. A **57**, 1448 (1998).
[16] M. Nakamura, S. Kita, and T. Hasegawa, J. Phys. Soc. Jpn **56**, 3161 (1987).
[17] H. Tanuma, S. Kita, I. Kusunoki, and N. Shimakura, Phys. Rev. A **38**, 5053 (1988).
[18] S. Kita, H. Tanuma, and M. Izawa, Chem. Phys. **125**, 415 (1988).
[19] S. Kita, T. Hasegawa, A. Kohlhase, and H. Inouye, J. Phys. B **20**, 305 (1987).
[20] W. Shepper, U. Ross, and D. Beck, Z. Physik A **290**, 131 (1979).
[21] H. J. Korsch and R. Schinke, J. Chem. Phys. **75**, 3850 (1981).
[22] S. Bosanac, Phys. Rev. A **22**, 2617 (1980).

[23] J. N. Harvey, Phys. Chem. Chem. Phys. **9**, 331 (2007).
[24] J. T. Muckerman, J. Chem. Phys. **54**, 1155 (1971).
[25] H. Inouye, M. Izawa, S. Kita, K. Takahashi, and Y. Yamato, Bull. Res. Inst. Sci. Meas. Tohoku, Univ. **32**, 41 (1984) [in Japanese].
[26] M. Izawa, S. Kita, and H. Inouye, J. Appl. Phys. **53**, 4688 (1982).
[27] S. Kita and H. Inouye, J. Mass Spectrom. Soc. Jpn **41**, 211 (1993) [in Japanese].
[28] H. Inouye, K. Niurao, and S. Kita, Chem. Phys. Lett. **33**, 241 (1975).
[29] E. W. McDaniel, in *Collision Phenomena in Ionized Gases* (John Wiley & Sons, New York, 1964), Chap. 1, pp. 2–10.
[30] K. P. Huber and G. Herzberg, in *Molecular Spectra and Molecular Structure: IV. Constants of Diatomic Molecules* (Van Nostrand Reinhold, New York, 1979).
[31] F. R. Gilmore, J. Quant. Spectrosc. Radiat. Transfer **5**, 369 (1965).
[32] F. An, S. Han, X. Hu, D. Xie, and H. Guo, Phys. Chem. Chem. Phys. **21**, 8645 (2019).
[33] D. Lu and H. Guo, J. Phys. Chem. A **127**, 3190 (2023).
[34] M. Waldman and R. G. Gordon, J. Chem. Phys. **71**, 1325 (1979).
[35] T. Ishikawa, S. Kita, and H. Inouye, Bull. Res. Inst. Sci. Meas. Tohoku, Univ. **24**, 1 (1975) [in Japanese].
[36] E. Clementi, IBM J. Res. Dev. **9**, 2 (1965); J. B. Mann, private communication (1971).
[37] S. Kita, K. Noda, and H. Inouye, Chem. Phys. **7**, 156 (1975).
[38] U. Gierz, J. P. Toennies, and M. Wilde, Chem. Phys. Lett. **110**, 115 (1984).
[39] M. Nakamura and A. Ichimura, Phys. Rev. A **71**, 062701 (2005).
[40] U. Buck, D. Otten, R. Schinke, and D. Poppe, J. Chem. Phys. **82**, 202 (1985).
[41] A. Ichimura and M. Nakamura, Phys. Rev. A **69**, 022716 (2004).
[42] H. Nakamura, in *Chemical Reaction Dynamics*, edited by H. Sano and T. Tominaga (Asakura-Shoten, Tokyo, 2004), p. 127 [in Japanese]; H. Kamisaka, W. Bian, K. Nobusada, and H. Nakamura, J. Chem. Phys. **116**, 654 (2002).
[43] S. Kita, S. Gotoh, T. Hasegawa, and N. Shimakura, J. Chem. Phys. **109**, 9713 (1998).
[44] P. J. Martin, E. Clemens, L. Zehnle, and V. Kempter, Z. Physik A **289**, 373 (1979).
[45] S. Kita, K. Shimizu, and N. Shimakura, J. Phys. Soc. Jpn **88**, 104301 (2019).
[46] A. Danjo and F. Koike, Phys. Rev. Lett. **62**, 741 (1989); F. Koike, private communication (2023).
[47] Y. Sato, M. Kikuchi, and H. Inouye, Phys. Rev. A **25**, 3376 (1982).